

Full length article

Lanthanide tetrads with implications for liquid immiscibility in an evolving magmatic-hydrothermal system: Evidence from rare earth elements in zircon from the No. 112 pegmatite, Kelumute, Chinese Altai



Zheng-Hang Lv, Hui Zhang*, Yong Tang

Key Laboratory of High-temperature and High-pressure Study of the Earth's Interior, Institute of Geochemistry, Chinese Academy of Sciences, Guiyang 550002, China

ARTICLE INFO

Keywords:

Lanthanide tetrads
Liquid immiscibility
Magmatic-hydrothermal system
Zircon
Pegmatite

ABSTRACT

The lanthanide tetrad effect and Y-Ho fractionation are commonly observed in highly fractionated melts. In pegmatites, they are attributed to liquid immiscibility, although this explanation has recently been debated. Based on the potential relationship between the lanthanide tetrad effect and liquid immiscibility in pegmatite-forming melts, the rare earth element compositions (REEs, including Y) in three types of zircons from the magmatic stage (Zone II), magmatic-hydrothermal transition stage (Zones III and V) and hydrothermal stage (Zone VI) of the Kelumute No. 112 pegmatite, Chinese Altai, were analyzed by laser ablation inductively coupled plasma mass spectrometry (LA-ICP-MS) in this study. The results show that the REEs are sharply fractionated from the magmatic stage to the hydrothermal stage. According to the REE variations in the three types of zircons that formed during different stages and the evidence from inclusions, the intense lanthanide tetrad effect and suprachondritic Y/Ho ratios in zircons from Zones III, V and VI result from selective incorporations of REEs in immiscible fluoride melt, which generated the W-type tetrad effect and subchondritic Y/Ho ratios in the fluoride melt and the complementary M-type tetrad effect and suprachondritic Y/Ho ratios in the coexisting silicate melt and aqueous fluid. The results further reflect that the liquid immiscibility of the silicate melt, fluoride melt and aqueous fluid occurred during the magmatic-hydrothermal transition stage of the pegmatite-forming melt. In addition, for the first time, a negative Ce anomaly was identified in the terrestrial zircon from Zone VI of the No. 112 pegmatite; this anomaly is attributed to the preferential incorporation and/or adsorption of Ce in/by the Fe-Mn oxyhydroxides prior to or during the crystallization of zircon in the hydrothermal stage.

1. Introduction

Pegmatites have been scrutinized for nearly two centuries because they are arguably among the most complex rocks known on Earth (London, 2008). The genesis of granitic pegmatite (hereafter referred to simply as pegmatite), which is commonly known to produce rare metal deposits, has been intensely investigated and debated. For example, Jahns and Burnham (1969) suggested that the saturation of the aqueous vapor phase and alkali fractionation between the melt and vapor give rise to mineral textural zoning in pegmatite. In contrast, London and co-workers proposed that the contributions of volatiles to pegmatite formation are limited but that melt undercooling and constitutional zone refining (CZR) are the core steps in the internal zonation in pegmatite (London, 2005, 2008, 2014). The magmatic-hydrothermal evolution process of pegmatite-forming melts includes the early magmatic stage, the magmatic-hydrothermal transition stage and the late hydrothermal stage, which are widely supported by melt-fluid inclusions (London,

1986, 1992; Lu et al., 1996; Touret et al., 2007), mineral chemistry (Černý et al., 1985; Zhang et al., 2004; Liu and Zhang, 2005; Bakker and Elburg, 2006; Van Lichtervelde et al., 2009) and experiments (Veksler, 2002, 2004; London, 2005, 2014). Veksler (2004) defined the magmatic-hydrothermal transition as ‘a stage in the evolution of magmatic systems when, in the process of cooling, aluminosilicate melt (the major liquid of the magmatic stage) approaches a terminal multiple-saturated eutectic and the leading role in element transport and further (subsolidus) evolution of the system is taken over by other fluid phases of vapors and hydrothermal liquids’.

The lanthanide tetrad effect is defined as four convex (M-type) or concave (W-type) segments (La-Nd; Pm-Gd; Gd-Ho and Er-Lu) with three discontinuity points at Nd/Pm, Gd and Ho/Er in chondrite-normalized rare earth element patterns (Masuda et al., 1987). Compared to the rare W-type tetrad effect, the M-type tetrad effect is generally observed in highly fractionated granites and pegmatites and are discrepantly attributed to (1) the fractional crystallization of REE-bearing

* Corresponding author.

E-mail address: zhanghui@vip.gyig.ac.cn (H. Zhang).<https://doi.org/10.1016/j.jseas.2018.05.031>Received 21 September 2017; Received in revised form 26 May 2018; Accepted 29 May 2018
Available online 30 May 2018

1367-9120/ © 2018 Elsevier Ltd. All rights reserved.

minerals (Zhao and Cooper 1993; McLennan, 1994; Pan, 1997; Pan and Breaks, 1997; Sha and Chappell, 1999; Duc-Tin and Keppler, 2015); (2) fluid-melt interactions (Irber, 1999; Dolejš and Štemprok, 2001; Zhao et al., 2002; Wu et al., 2011); (3) immiscibility between a vapor and coexisting fluid (Monecke et al. 2011) or alteration by the immiscible fluid (Monecke et al., 2002, 2007; Tang and Zhang, 2015); (4) immiscibility between silicate melt and hydrosaline melt/fluid before the formation of pegmatite-forming melt (Liu and Zhang, 2005; Cao et al., 2013); and (5) immiscibility between fluoride and silicate melts during the fractionation of pegmatite-forming melt (Veksler et al., 2005; Badanina et al., 2006). In pegmatite, the lanthanide tetrad effect has increasingly been attributed to various liquid immiscibility processes in recent years (Liu and Zhang, 2005; Veksler et al., 2005; Cao et al., 2013; Tang and Zhang, 2015). Therefore, the mechanism responsible for the lanthanide tetrad effect in pegmatite-forming melt is still under debate.

There is still no general consensus about the mechanism for immiscibility in pegmatite-forming melts. In addition to the immiscibility mechanisms mentioned above, several other mechanisms have been proposed. For example, London (1982, 1992 and 2008) proposed possible two-liquid or two-gel immiscibility at the end of the pegmatite-forming process based on inclusion and experimental petrology studies of the Tanco pegmatite, Canada. The study of the melt inclusions hosted by quartz from pegmatites implies the occurrence of immiscible F- and P-rich melts (Webster et al., 1997). Zhang (2001) suggested that the high enrichment of Be and P in the saccharoidal albite zone of the Koktokay No. 3 pegmatite, Chinese Altai, probably resulted from immiscibility between a P-rich melt and a silicate melt. Experiments by Veksler et al. (2002, 2004) documented the coexistence of three immiscible phases, including an aluminosilicate melt, a hydrosaline melt and an aqueous fluid, in a synthetic pegmatite melt. Thomas and co-workers suggested the occurrence of three immiscible phases, i.e., a peraluminous and less water-rich melt (type-A), a conjugate water-rich peralkaline melt (type-B) and a coexisting fluid phase, in a highly fractionated pegmatite-forming melt (Thoams et al., 2006, 2011; Thomas and Davidson, 2008, 2012). The study of REE ore deposits hosted by pegmatite from Strange Lake, Canada, indicated that immiscibility between fluoride and silicate melts has an important role in REE ore formation (Vasyukova and Williams-Jones, 2014).

Based on the potential relationship between the lanthanide tetrad effect and liquid immiscibility in pegmatite-forming melts, the compositions of rare earth elements (REEs, including Y) in zircons from the four textural zones of the No. 112 pegmatite, Kelumute, Chinese Altai, were analyzed via laser ablation inductively coupled plasma mass spectrometry (LA-ICP-MS) in this work, in order to reveal the mechanism responsible for the lanthanide tetrad effect and to classify the liquid immiscibility that occurred during the magmatic-hydrothermal evolution of the pegmatite-forming melts.

2. Geological background

The Chinese Altai is located in northwestern China and consists of nine pegmatite fields and more than 100,000 pegmatites (Wu and Zou, 1989). The Kelumute No. 112 pegmatite is the largest and richest dyke in the Kelumute-Jideke pegmatite field and hosts a large-scale rare metal (Li-Be-Nb-Ta) ore deposit, which is second in reserve and scale only to the Koktokay No. 3 pegmatite in the Chinese Altai. There are hundreds of pegmatite dykes exposed in the pegmatite field, and some of them host various scales of Be, Be + Nb + Ta and Li + Be + Nb + Ta deposits. Igneous rocks are widely exposed in the Kelumute-Jideke pegmatite field, including a peripheral granodiorite, a biotite granite, a fine-grained gneissic two-mica granite and a two-mica granite (Fig. 1). The biotite granite and gneissic two-mica granite are the main wall rocks of pegmatite in the field and have zircon U-Pb ages of 456 Ma and 446 Ma, respectively. The Kelumute No. 112 pegmatite directly intruded into the gneissic two-mica granite ca. 238 Ma (Lv et al., 2012). The Silurian Upper Habahe group crops out sporadically

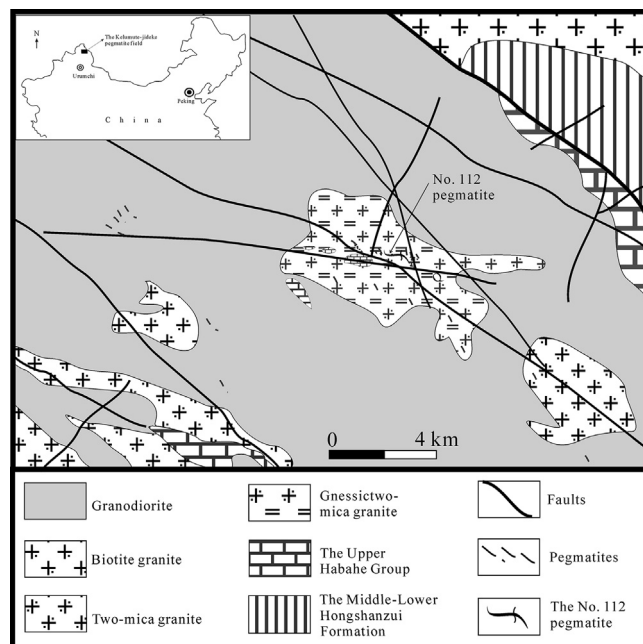


Fig. 1. Geological map of Kelumute–Jideke pegmatite field, showing the occurrence of the Kelumute No. 112 pegmatite (Modified according to Lv et al., 2012).

in the field with small-scale outcrops composed of biotite-quartz schist and banded migmatite. The Carboniferous Middle and Lower Hongshanzui formations are mainly exposed in the northeastern part of the field and comprise metavolcanic rock, tuff, argillite and siltstone. Three main sets of faults with EW, NW and NE strikes have been identified in the mining area. The EW- and NW-striking faults are ore-capacity faults filled by pegmatites, with lengths of hundreds to thousands of meters and widths of several to dozens of meters. The NE-striking faults belong to post-metallogenetic fault that are less than one hundred meters in length and less than ten meters in width (Fig. 1).

The pegmatite vein is S-shaped, 1380 m in length and 3 to 12 m in width. Cut by two faults, it is divided into eastern, middle and western parts, with NW, N and NE strikes and dip angles of 40°, 50° and 45°, respectively (Fig. 2). The mineralization grades are different in the three parts: the richest is in the middle, and the poorest is in the west. The western part is wedge-like, with a length of 280 m and a horizontal thickness varying from 2.5 m (east) to 4 m (west). The middle part is bed-like and is approximately 660 m long and 7 m wide. The eastern part is also bed-like and is 440 m long and 5.5 m wide on average (Fig. 2). Based on macroscopic textures and different mineral associations, the No. 112 pegmatite vein was divided into the following six textural zones (Lv et al., 2012): an albitization microcline-quartz-albite zone (I), which accounts for 20 vol% of the No. 112 pegmatite and is present along the hanging wall and footwall as continuous bands; an albitization blocky microcline zone (II), which accounts for 5 vol% of the pegmatite and shows a nest-like or banded distribution along the hanging wall; a quartz-albite-spodumene zone (III), which accounts for 60 vol% of the pegmatite and presents as continuous bands in the middle zone or along the hanging wall and footwall of the vein; an albite-quartz-muscovite zone (IV), which accounts for 2 vol% of the pegmatite and presents as small nest- or vein-like occurrences that are sporadically hosted in zones I, II and III; a saccharoidal albite zone (V), which accounts for 12 vol% of the pegmatite and presents as individual, cluster or nest-like distributions; and a quartz core zone (VI), which accounts for a small proportion (~1 vol%) of the pegmatite vein and exhibits a random nest-like distribution in the center of the middle segment of the vein. The distributions of rock-forming and accessory minerals in the different texture zones of the Kelumute No. 112

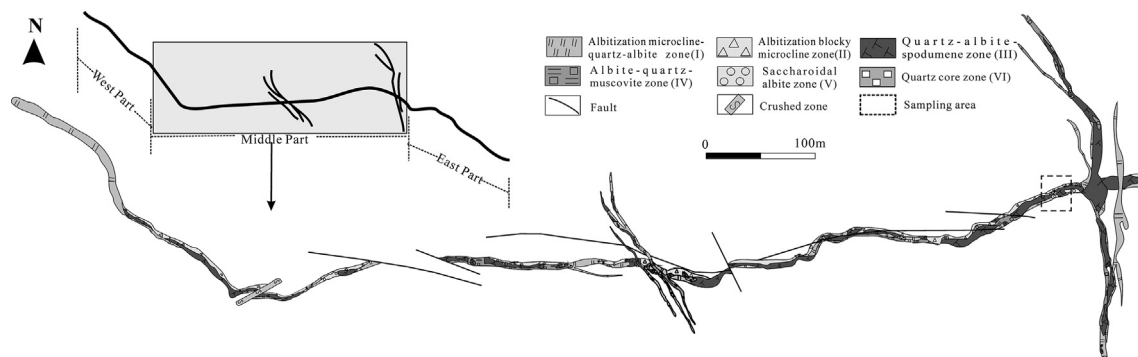


Fig. 2. Geological map of six mineral textural zones of the middle part of Kelumute No. 112 pegmatite (Modified according to Lv et al., 2012).

Table 1

Distribution of rock-forming and accessory minerals in the Kelumute No. 112 pegmatite.

Mineral textural zone	Zone I	Zone II	Zone III	Zone IV	Zone V	Zone VI	UM
quartz	30	25	30	30	10	99	wt%
albite	37	10–15	35	25	86	++	
microcline	28	45–60	5	15–20	+	++	
muscovite	2–3	1–2	3	20	2	++	
spodumene	+	+	25–30	+	+	–	
Nb-Ta oxide	230	143–268	153–300	38	231	+	g/t
apatite	179	257–383	54–206	1130	188–638	+	
spessartite	200	74–1507	3–143	31	18–156	–	
zircon	35	10	3–22	9	17–43	++	
limonite	68	93	126	26	20–61	+++	
Fe-Mn oxyhydroxides	++	+	1–18	191	2–16	++	
bismutite	9	31–142	5–88	+	3	+	
microlite	+	+	+	+	4–62	+	
lithiophilite	–	–	3–21	–	+++	–	
beryl	++	+	+++	+++	+++	–	
grossularite	+	+	–	+	–	–	
tourmaline	+	+	+	–	+	–	
topaz	–	–	+	–	+	–	
cryolite	–	–	+	–	+	–	
calcite	+	+	+	+	–	+	
magnetite	++	++	+	+	+	–	
monazite	–	–	+	–	+	–	
xenotime	–	–	+	–	+	–	
rutile	+	+	–	–	–	–	
titanite	+	+	–	–	–	–	
ilmenite	+	–	–	–	–	–	

Note: UM = unit of measurement. The symbols + + +, + +, + and – mean abundant, present, rare and not observed, respectively. Modified according to Zou et al. (1981).

pegmatite are presented in Table 1. Based on the mineral chemistry (Zou et al., 1981), inclusions (Wu et al., 1994; Lv, 2013) and U-Pb geochronology of the zircons (Lv et al., 2012), it has been suggested that Zones I and II formed at the magmatic stage (233–238 Ma), Zones III and V are formed at the magmatic-hydrothermal transition stage (219 Ma), and Zone VI are formed at the late hydrothermal stage (211 Ma). Zone IV represents a replacement unit of Zones I and II by exsolved hydrothermal fluid.

3. Samples and analytical methods

Four rock samples, K2, K3, K5 and K6, were collected from Zones II, III, V and VI, respectively, in the middle part of the No. 112 pegmatite (Fig. 2), based on the mineral assemblage of the six textural zones. The zircon grains were concentrated by flotation and magnetic separation and were handpicked under a binocular microscope. Zircon target preparation, cathodoluminescence (CL) image acquisition, and in situ trace element analysis by laser ablation inductively coupled plasma mass spectrometry (LA-ICP-MS) were conducted at the State Key Laboratory of Continental Dynamics, Department of Geology at Northwest University, China. The laser ablation system was a GeoLas 200 M with

wavelength of 193 nm, a maximum energy of 200 mJ and a maximum pulse rate of 20 Hz that was equipped with an Agilent7500a ICP-MS. The working conditions were as follows: laser frequency, 10 Hz; laser energy, 80 mJ; beam diameter, 32 μ m; ablation depth, 20–40 μ m; and background and analytical signal acquisition, 30 s and 50 s, respectively. Helium was used as the carrier gas to enhance the transport efficiency of the ablated materials (Yuan et al., 2004). NIST SRM610 glass and GJ-1 zircon were used as the external standard and monitoring samples, respectively (Pearce et al. 1997; Black et al. 2004), and ^{29}Si was used as an internal standard (Anczkiewicz et al., 2001) to calibrate and normalize the concentrations of the trace elements. Based on choosing the smooth background and analytical signals, quantitative calibration and time-drift corrections for the trace element analyses were performed using the GLITTER 4.0 algorithm (Macquarie University). Most of the analyzed trace element concentrations of the zircon samples were 2 or 3 orders of magnitude higher than the detection limit of the instrument, and the relative errors of the analysis were mostly less than 5%. In addition, the trace element compositions of Fe-Mn oxyhydroxides from the quartz core (Zone VI) of the No. 112 pegmatite were analyzed at the State Key Laboratory of Ore Deposit Geochemistry at the Institute of Geochemistry, Chinese Academy of

Sciences (IGCAS), using an Agilent 7500a ICP-MS and both NIST SRM610 and GSE-1G as external standards. Quantitative calibration and time-drift corrections for the trace element analyses were performed using ICPMSDataCal 10.8 (Liu et al., 2008).

Laser Raman spectra of minerals were collected using a Renishaw in Via plus laser Raman microscope at the Key Laboratory of High-temperature and High-pressure Study of the Earth's Interior, IGCAS. Excitation was achieved using an argon-ion laser tuned to 514.5 nm. The laser beam diameter was 2 μm , and the instrumental resolution was better than 2 cm^{-1} . The laser intensity was 5 mW, the beam was coupled with a grating of 1800 grooves per mm, and the collection time was 20 s.

4. Results

4.1. Zircon morphology, cathodoluminescence (CL) and Raman spectrum

Zircons from Zone II vary in size from 250 to 500 μm , are brown, translucent or opaque, and have an euhedral habit of tetragonal-dipyramid {1 1 1} and/or stubby tetragonal prism {1 1 0}. Most of the zircons show dark and mottled inner areas and residual rims with oscillatory zoning. Some bright areas with intense cathodoluminescence (CL) are locally observed in the residual zircon rim (Fig. 3a). The mottled inner areas have three main Raman shifts at 344 cm^{-1} , 436 cm^{-1} and 997 cm^{-1} , with corresponding FWHMs (full width at half maximum) of 18 cm^{-1} , 18 cm^{-1} and 17 cm^{-1} , respectively. The residual rims have three main Raman shifts at 350 cm^{-1} , 437 cm^{-1} and 1005 cm^{-1} , with corresponding FWHMs of 11 cm^{-1} , 9 cm^{-1} and 6 cm^{-1} , respectively. The bright areas have three main Raman shifts at 351 cm^{-1} , 438 cm^{-1} and 1007 cm^{-1} , with corresponding FWHMs of 9 cm^{-1} , 8 cm^{-1} and 4 cm^{-1} , respectively (Fig. 3e; Table 2).

Zircons from Zone III show sizes of 200 to 400 μm , are dark brown and opaque, and have a subhedral habit of tetragonal-dipyramid {1 1 1} or euhedral habit of stubby tetragonal prism {1 1 0}. Most zircons show mottled inner areas, residual rims with broadened and dark oscillatory zoning and homogeneous dark areas (Fig. 3b). The mottled inner areas have three main Raman shifts at 346 cm^{-1} , 436 cm^{-1} and 1000 cm^{-1} , with corresponding FWHMs of 14 cm^{-1} , 12 cm^{-1} and 13 cm^{-1} ,

respectively. The residual rims and homogeneous dark areas have similar Raman features; their main shifts are observed at 351 cm^{-1} , 438 cm^{-1} and 1006 cm^{-1} , with corresponding FWHMs of 7 cm^{-1} , 8 cm^{-1} and 6 cm^{-1} , respectively (Fig. 3f; Table 2).

Zircons from Zone V have sizes of 100–300 μm , are gray and translucent, and have a subhedral habit of tetragonal-dipyramid {1 1 1} or euhedral habit of stubby tetragonal prism {1 1 0}. Most zircons consist of dark, mottled and/or fissured inner areas and residual rims with broadened and dark oscillatory zoning in the CL images. Some zircons have bright areas with intense CL in the rim of zircon. The mottled inner areas have three main Raman shifts at 349 cm^{-1} , 437 cm^{-1} and 1002 cm^{-1} , with corresponding FWHMs (full width at half maximum) of 16 cm^{-1} , 15 cm^{-1} and 12 cm^{-1} , respectively. The residual rims have three main Raman shifts at 351 cm^{-1} , 438 cm^{-1} and 1006 cm^{-1} , with corresponding FWHMs of 8 cm^{-1} , 9 cm^{-1} and 6 cm^{-1} , respectively. The bright areas have three main Raman shifts at 352 cm^{-1} , 438 cm^{-1} and 1007 cm^{-1} , with corresponding FWHMs of 7 cm^{-1} , 8 cm^{-1} and 5 cm^{-1} , respectively (Fig. 3g; Table 2).

Zircons from Zone VI show sizes of 150–350 μm , are dark brown and translucent, and have a subhedral habit of tetragonal-dipyramid {1 1 1} or euhedral habit of stubby tetragonal prism {1 1 0}. None of the zircons have oscillatory zoning, and most show mottled inner areas with weak CL and dark homogenous rims in the CL images. The mottled inner areas have three main Raman shifts at 345 cm^{-1} , 435 cm^{-1} and 1001 cm^{-1} , with corresponding FWHMs of 17 cm^{-1} , 15 cm^{-1} and 13 cm^{-1} , respectively. The rims show Raman shifts at 354 cm^{-1} , 438 cm^{-1} and 1006 cm^{-1} , with corresponding FWHMs of 10 cm^{-1} , 11 cm^{-1} and 7 cm^{-1} , respectively (Fig. 3h; Table 2).

The CL features and Raman spectrum of zircon have been systematically studied (Corfu et al., 2003; Nasdala et al., 2003). The former can reflect variations in the abundances of trace elements (e.g., U and Y) and defects in the crystal lattice of zircon. The latter is used as a powerful technique to quantify the order degree of crystal structures. The Raman spectrum of zircon is dominated by internal vibrations of SiO_4 tetrahedrons and characterized by three main bands at 356, 439 and 1008 cm^{-1} (Nasdala et al., 2003). These bands and their corresponding FWHMs commonly decrease and broaden, respectively, with increasing radiation damage. Thereinto, the FWHM of the intense ν_3

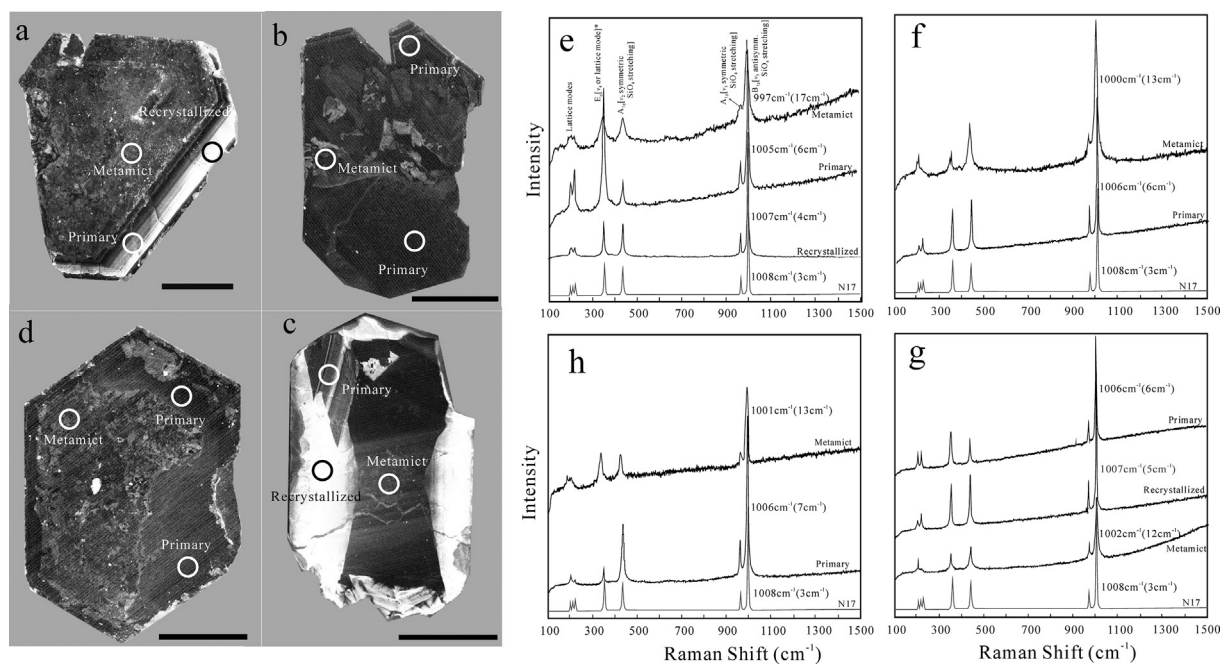


Fig. 3. Representative cathodoluminescence (CL) images (a–d) and corresponding Raman spectra (e–h) of zircons from zones II, III, V and VI of Kelumute No. 112 pegmatite, respectively. LA-ICPMS analytic areas are collected according to CL and Raman spectra. Values in Raman figures represent shift values of ν_3 and corresponding full width at half maximum (FWHM). Scale bars correspond to 100 μm .

Table 2

The parameters of the Raman bands of representative zircons from the Kelumute No. 112 pegmatite.

Zircon sample and type	E_g (tetrahedron rotation, ν_4)			A_{1g} (symmetric bending, ν_2)			B_{1g} (antisymmetric stretching, ν_3)		
	ν (cm^{-1})	FWHM (cm^{-1})	I (counts)	ν (cm^{-1})	FWHM (cm^{-1})	I (counts)	ν (cm^{-1})	FWHM (cm^{-1})	I (counts)
K2 (Zone II)									
PA	350	11	5395	437	9	2003	1005	6	6610
RA	351	9	1621	438	8	1632	1007	4	7192
MA	344	18	2041	436	18	2004	997	17	3950
K3 (Zone III)									
MA	347	14	1349	436	12	2265	1000	13	5378
PA	351	7	2472	438	8	2801	1006	6	7625
K5 (Zone V)									
PA	351	8	2877	438	9	2279	1006	6	9649
RA	352	7	2991	438	8	2187	1007	5	9382
MA	349	16	2643	437	15	2897	1002	12	5476
K6 (Zone VI)									
MA	345	17	2203	435	15	2136	1001	13	3936
PA	354	10	2103	438	11	2298	1006	7	7891

Abbreviation: FWHM = full width at half maximum; MA = metamict area; RA = recrystallized area; PA = primary area.

(SiO_4) mode at 1008 cm^{-1} is mostly sensitive to structure defects and is used in zircon study to estimate the degree of metamictization (Nasdala et al., 1998). According to these features, three types of areas of zircon from the No. 112 pegmatite, primary area (PA), metamict area (MA) and recrystallized area (RA), can be identified. The primary area represents the first crystallization product of zircon and shows concordant and the oldest U-Pb age in the same textural zone (Lv et al., 2012), residual oscillatory zoning (Fig. 3a, b and c) or homogeneous and weak CL (Fig. 3b and d). The typical bands at 356 cm^{-1} , 439 cm^{-1} and 1008 cm^{-1} (with FWHMs of 6 cm^{-1} , 7 cm^{-1} and 3 cm^{-1} , respectively) for very well crystallized zircon (such as the gemstone-quality zircon N17 from Sri Lanka, Nasdala et al., 2002) are observed at $352\text{--}354 \text{ cm}^{-1}$, $436\text{--}438 \text{ cm}^{-1}$ and $1005\text{--}1007 \text{ cm}^{-1}$ in the zircon PAs (Fig. 3e–h; Table 2), with corresponding FWHMs of $11\text{--}7 \text{ cm}^{-1}$, $11\text{--}8 \text{ cm}^{-1}$ and $8\text{--}5 \text{ cm}^{-1}$, respectively. These features indicate that the PAs are moderate to well crystallized and avoided late metamictization and recrystallization. The metamict area is formed by radiation damage after zircon crystallization due to high U \pm Th abundance (Wu and Zheng, 2004). It commonly shows a discordant U-Pb age (Lv et al., 2012), a spongy or mottled structure, an enrichment of inclusions and weak CL due to defects in the crystal lattice (Fig. 3a–d). For the MAs, three typical bands are observed at $344\text{--}350 \text{ cm}^{-1}$, $434\text{--}436 \text{ cm}^{-1}$ and $996\text{--}1002 \text{ cm}^{-1}$, with evidently broadened FWHMs of $18\text{--}14 \text{ cm}^{-1}$, $18\text{--}12 \text{ cm}^{-1}$ and $17\text{--}12 \text{ cm}^{-1}$ (Fig. 3e–h; Table 2), indicating that they experienced metamictization. Recrystallized areas result from the intra-grain ‘recovering’ of previously formed zircon under certain *P-T* conditions (usually $\geq 400 \text{ }^\circ\text{C}$) (Wu and Zheng, 2004). Unstable areas of zircon, including the rim, the metamict area and the area around mineral inclusion or areas enriched in nonformula elements, are preferably affected by recrystallization (Pidgeon, 1992). The RA generally has a concordant U-Pb age that is younger than the crystallization age obtained from the PAs (Lv et al., 2012), a patchy structure and intense CL (Fig. 3a and c) due to the exclusion of nonformula trace elements (such as U, Th and REE) and recovered crystal lattice. Three typical bands are observed at $354\text{--}355 \text{ cm}^{-1}$, $437\text{--}438 \text{ cm}^{-1}$ and $1006\text{--}1007 \text{ cm}^{-1}$, with corresponding FWHMs of $8\text{--}7 \text{ cm}^{-1}$, $7\text{--}8 \text{ cm}^{-1}$ and $7\text{--}5 \text{ cm}^{-1}$, respectively (Fig. 3e and g; Table 2). These features prove that the RAs are well crystallized.

4.2. Rare earth elements in zircon

Fifteen zircons from Zone II have REE contents ranging from 5 ppm to 14421 ppm, and the PAs, MAs and RAs have contents of 55–2120 ppm, 1598–14421 ppm and 5–998 ppm, respectively

(Table 3). The zircons commonly show heavy rare earth element (HREE)-enriched REE patterns, with a peak at Gd or Ho, an evident positive Ce anomaly ($\delta \text{Ce} = 1.07\text{--}3.92$, except for two MAs that show low values of 0.75 and 0.84) and a negative Eu anomaly ($\delta \text{Eu} = 0.40\text{--}0.54$) (Table 4; Fig. 4a). Only one RA shows slight M-type REE tetrad effects in its HREE segment, with t3, t4 and $\text{TE}_{3,4}$ values of 1.23, 1.18 and 1.20, respectively (point 20, Table 3). The zircon PAs, MAs and RAs have Y/Ho ratios of 34–46, 37–50 and 36–42, respectively.

Sixteen zircons from Zone III have REE contents ranging from 12 ppm to 341 ppm, and the PAs and MAs have contents of 12–168 ppm and 35–341 ppm, respectively (Table 3). The zircons commonly show HREE-enriched patterns with significant M-type REE tetrad effects (Fig. 4b). Most of the zircons have a positive Ce anomaly ($\delta \text{Ce} = 1.05\text{--}3.07$), and a few zircons have a negative Eu anomaly ($\delta \text{Eu} = 0.27\text{--}0.41$). The PAs and MAs have $\text{TE}_{3,4}$ values of 1.36–1.99 and 1.53–2.06, respectively (Table 3) and Y/Ho ratios of 72–195 and 58–221, respectively.

Fourteen zircons from Zone V have REE contents ranging from 5 ppm to 53 ppm, and the PAs, RAs and MAs have contents of 8–34 ppm, 5–11 ppm and 16–53 ppm, respectively (Table 3). The zircons commonly show HREE-enriched patterns with a significant depletion of LREEs (light rare earth elements) and M-type REE tetrad effects (Fig. 4c). Most of the zircons have indistinguishable Ce and Eu anomalies due to the extremely low LREE abundance (below the detection limit), and the analytical spots of only three PAs and one MA show calculable $\text{TE}_{3,4}$ values of 1.38–1.77 and 1.26. The PAs, MAs and RAs have Y/Ho ratios of 62–154, 51–78 and 88–255, respectively (Table 3).

Sixteen zircons from Zone VI have REEs contents ranging from 299 ppm to 7160 ppm, and the PAs and MAs have contents of 355–7160 ppm and 299–6799 ppm, respectively (Table 3). The zircons show HREE-enriched patterns for the PAs and flat patterns for the MAs (Fig. 4d). Both types have intense negative Ce anomalies ($\delta \text{Ce} = 0.01\text{--}0.47$), evident negative Eu anomalies ($\delta \text{Eu} = 0.17\text{--}0.47$) and significant M-type REE tetrad effects. The PAs and MAs have Y/Ho and $\text{TE}_{3,4}$ values of 47–69 and 1.31–1.91 and 36–59 and 1.13–1.59, respectively (Table 3).

5. Discussion

Generally, REEs are incorporated into zircon due to their similar ionic radiuses (from the 1.160 \AA radius of La to the 0.997 \AA radius of Lu for octahedral coordination, Shannon, 1976) to that of Zr^{4+} (0.84 \AA) (Hoskin and Schaltegger, 2003). The dominant REE substitution

Dulski, 1995; Bau, 1996; Irber, 1999; Liu and Zhang, 2005). In highly evolved granitic and pegmatitic melts, the increase in the M-type tetrad effect is always accompanied by the increasing fractionation of Y-Ho (Irber, 1999; Liu and Zhang, 2005), which therefore indicates that the mechanism responsible for the lanthanide tetrad effect should also explain the fractionation of Y-Ho (Irber, 1999).

5.1. REE features in different types of zircon

In general, the MAs of the zircon from the No. 112 pegmatite have high REE, U and Th contents, the PAs have lower REE, U and Th contents than the MAs and the RAs have the lowest REE (Table 3, Fig. 4), U and Th contents (Lv et al., 2012). The high contents in the zircon MAs can be attributed to the (1) variation in the abundance of these elements during zircon crystallization. As shown in Fig. 3, metamictization is commonly observed in the core area of zircon, indicating the core has a higher abundance of these elements than the rim of zircon (Zhang et al., 2003); and (2) the lattice expansion and metamictization, which facilitate the incorporation of nonformula elements (especially LREEs) into zircon during late fluid alteration (Hoskin and Schaltegger, 2003; Zeng et al., 2017). The low contents in the zircon RAs are ascribed to the exclusion of nonformula elements during the recovering process induced by recrystallization (Hoskin and Schaltegger, 2003). Comparatively, the PAs have intermediate contents of trace elements due to limited effects from metamictization and recrystallization.

On basis of the PAs, the variations in chondrite-normalized REE patterns of the MAs and RAs should result from alteration by late hydrothermal fluid and the elemental exchange between zircon and late melt/fluid during recrystallization, respectively. For example, a few zircon MAs from Zones II and III show a weakened Ce anomaly, an increased LREE content and a decreased HREE content compared to the PAs (Fig. 4a, b), indicating they may have been altered by the late hydrothermal fluid from which Zone VI crystallized. Some zircon RAs from Zone II have a slight lanthanide tetrad effect, indicating the participation of late hydrothermal fluid during recrystallization. The wide range of the total REE content in zircons from Zone II may reflect the rapid crystallization of the Zone due to large thermal gap between the pegmatite melt and wall rock and the slow diffusion rate of REEs in melt (London, 2008). The comparative depletion of HREEs in the zircon from Zone II could be attributed to the crystallization of abundant HREE-rich spessartite (Table 1; Fig. 6) prior to zircon formation, which is similar to the competitive partitioning between zircon and paragenetic garnet in metamorphic rocks (Schaltegger et al., 1999).

The zircons from Zones II, V and VI of the No. 112 pegmatite have been dated at 234 Ma, 219 Ma and 211 Ma by U-Pb dating, respectively. However, the zircons from Zone III show ages ca. 188 Ma (Lv et al., 2012). A similar situation is also observed in the Koktokay No. 3 pegmatite. The zircons in Zones I, V and VII from the Koktokay pegmatite have zircon U-Pb ages of 220 Ma, 198 Ma and 213 Ma, respectively (Wang et al., 2007). The younger ages of the zircons from the intermediate zone of pegmatite are attributed to the fluid alteration in the late hydrothermal stage (Wang et al., 2007; Lv et al., 2012). We suggest that the Zone III formed during the magmatic-hydrothermal transition stage, and the zircon PAs from this zone retain more primary REE features than the MAs, based on the following evidence: (1) abundant melt-fluid inclusions in the spodumene from Zone III of the No. 112 pegmatite (Wu et al., 1994; Lv, 2013) and Zone V from the No. 3 pegmatite (Lu et al., 1996) indicate that both zones formed at the magmatic-hydrothermal stage; and (2) the zircon RAs from Zone II have similar 'reworked' age of 186 Ma to the age (188 Ma) of zircon from Zone III; (3) the REE pattern of the zircon PAs from Zone III is characterized by evident LREE depletion and HREE enrichment, which contrasts to the flat HREE pattern of the zircon MAs (Fig. 4b); (4) the zircon MAs from Zone III have a similar HREE pattern as the zircon from Zone VI, indicating they are evidently altered by late fluid; and (5) previous studies have demonstrated that Pb has a faster diffusion rate

than REE, U and Th in zircon, and radiation damage may enhance its diffusion rate (Cherniak et al., 1997; Lee et al., 1997). Therefore, hydrothermal alteration has a larger effect on the zircon U-Pb age than REEs (Geisler et al., 2003).

The evidently decreasing content of REEs in the zircons from Zones III and V might have been induced by competitive partitioning between zircon and paragenetic REE-rich minerals or by the extraction of REEs from silicate melt by the immiscible phase. However, the former could be excluded by the consistent REE contents in the paragenetic spessartite, apatite and Nb-Ta group minerals from Zones II, III and V (Fig. 6; and our unpublished data). In addition, the paragenetic zircons with abundant monazite and xenotime from the Jiangjunshan and Qiemoerqieke pegmatites, Chinese Altai, have high REE contents that are 2–3 orders of magnitude higher than those of the zircons from Zones III and V in the No. 112 pegmatite (our unpublished data). Our recent work reveals that the zircons from Zones IV and V of the Koktokay No. 3 pegmatite have low REE contents (our unpublished data) similar to those of the zircons from Zones III and V of the No. 112 pegmatite. However, rare earth phosphates are basically absent in Zones IV and V of the No. 3 pegmatite (Wang et al., 1981). Together, this evidence demonstrates that the fractional crystallization of rare earth phosphates may not be the cause of the extremely low REEs in zircon. Similar to Zones III and V of the No. 112 pegmatite, Zones IV and V of the No. 3 pegmatite have been proven to have formed during the magmatic-hydrothermal stage (Lu et al., 1996; Zhang, 2001; Liu and Zhang, 2005). The extremely low REEs in zircons are probably associated with the occurrence of an immiscible REE-rich phase during the magmatic-hydrothermal stage of pegmatite-forming melt (see below).

In addition to the features mentioned above, the zircons from Zone II commonly lack the lanthanide tetrad effect in their REE patterns (Fig. 4a) and have similar Y/Ho ratios as those of the CHARAC field (Fig. 5a), indicating that the REEs are slightly fractionated during the magmatic stage. In comparison, zircons from Zones III and V have intense M-type tetrads (Fig. 4b and c), increasing Y/Ho ratios (Fig. 5a), and decreasing REEs (Fig. 5b), indicating the REEs were largely fractionated during the magmatic-hydrothermal transition stage. Although zircons from both zones have extremely low REE abundances, especially LREE abundances, the lanthanide tetrad effect can be distinguished from the HREE pattern (Fig. 4b and c) and quantized values of t3 and t4 (> 1.1, Table 3). In addition, similar REE features are also observed in the paragenetic minerals of the spessartite and apatite with the zircon from the No. 112 pegmatite. Both minerals from Zones I and II feature a high REE abundance and no lanthanide tetrad effect. However, those from Zones III and V have a low REE abundance and a significant lanthanide tetrad effect (Fig. 6). Zircons from Zone VI have a similar lanthanide tetrad effect and Y/Ho ratios as the zircons from Zones III and V (Fig. 5a). However, the negative Ce anomaly in those zircons (Fig. 4d) indicates the REEs are secondly fractionated in the hydrothermal stage. All these features indicate that the REEs in the Kelumute No. 112 pegmatite-forming melt are increasingly fractionated from the magmatic stage to hydrothermal stage. In addition, the variations in REEs (including variations in the lanthanide tetrad effect, Y/Ho ratios and Ce anomaly) in zircons from different zones may result from one more differentiated processes or mechanisms, which will be discussed below.

5.2. Lanthanide tetrad effect and liquid immiscibility

As mentioned above, several mechanisms have been proposed to explain the REE tetrad effect and non-chondritic Y/Ho ratios in granites and pegmatites. We try to use these mechanisms to explain the REE features in zircons as following:

- (1) Fractional crystallization of REE-bearing minerals. This mechanism suggests that the crystallization of REE-bearing minerals prior to zircon saturation gives rise to the M-type tetrad effect in residual

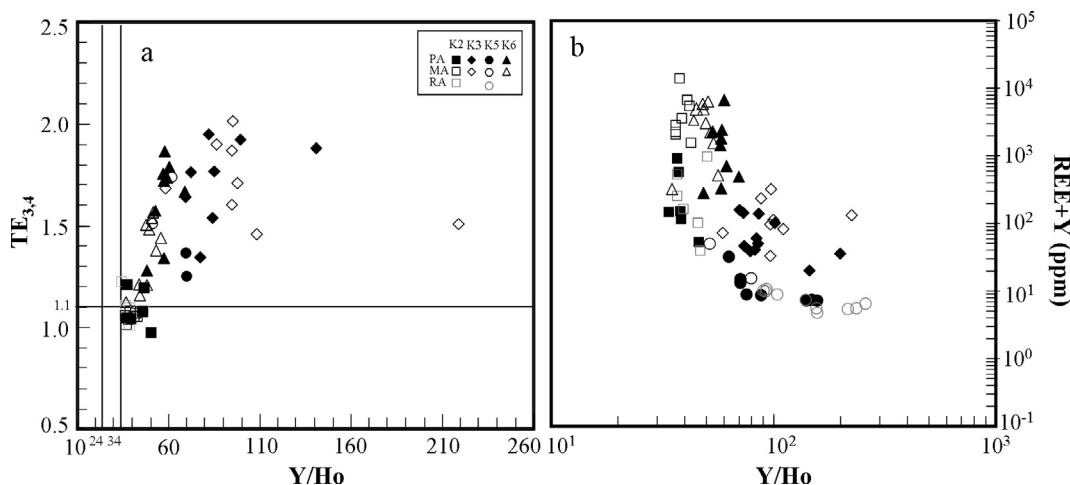


Fig. 5. Plot of $TE_{3,4}$ vs. Y/Ho showing a positive correlation between the tetrad effect and fractionation between Y and Ho (a) and total contents of REEs and Y vs. Y/Ho ratios (b) in zircon from the Kelumute No. 112 pegmatite. The degree of the lanthanide tetrad effect $TE_{3,4} = (t_3 \times t_4)^{1/2}$, $t_3 = (Tb_N / (Gd_N^{2/3} \times Ho_N^{1/3}) \times Dy_N / (Gd_N^{1/3} \times Ho_N^{2/3}))^{1/2}$, $t_4 = (Tm_N / (Er_N^{2/3} \times Lu_N^{1/3}) \times Yb_N / (Er_N^{1/3} \times Lu_N^{2/3}))^{1/2}$, denotes the third and fourth tetrad (Irber, 1999). CHARAC field defined a Y/Ho value range from 24 to 34 (Bau, 1996). K2, K3, K5 and K6 represent sample numbers of zones II, III, V and VI. Abbreviations of MA, PA and RA mean metamict area, primary area and recrystallized area, respectively.

melt and the co-existing minerals (Zhao and Cooper, 1993; McLennan, 1994; Pan, 1997). However, experiments have proven that the fractional crystallization of REE-rich accessory minerals, such as garnet, apatite or monazite, which are thought to generate REE tetrad effects in peraluminous melt, only give rise to Nd and Ho discontinuities, with no REE tetrad effect characteristics in the chondrite-normalized REE patterns of residual melts (Irber, 1999). In addition, apatite and garnet minerals from the Koptokay No. 3 pegmatite (Zhang, 2001; Liu and Zhang, 2005; Cao et al., 2013) and Kelumute No. 112 pegmatite (Fig. 6), Chinese Altai, all show similar REE features to the paragenetic zircons.

(2) Fluid-melt interaction. This mechanism proposes that an F-rich fluid phase with the W-type tetrad effect exsolved from the highly fractionated melt in an open system, which resulted in the complementary M-type tetrad effect in the residual melt (Irber, 1999; Dolejš and Štemprok, 2001; Zhao et al., 2002; Wu et al., 2011). However, the zircons from the quartz core (Zone VI) that precipitated from the exsolved hydrothermal fluid show significant M-type tetrad effects instead of W-type tetrad effects (Fig. 4d). In addition, hydrothermal fluorites from the exsolved fluid from the Li-F granite in Germany (Monecke et al., 2007) and the wall rocks altered by the exsolved fluid from the Koptokay No. 3 pegmatite in

the Chinese Altai (Zhang, 2001; Liu and Zhang, 2005), both show M-type tetrad effects.

(3) Immiscibility between a vapor and a coexisting liquid and alteration by the immiscible fluid. This mechanism suggests that the exsolved fluid splits into a high-salinity fluid and a coexisting CO_2 -rich, low-salinity vapor during the late hydrothermal stage. The preferential partitioning of REE-Cl in the fluid phase and the partitioning of REE-F complexes in the CO_2 -bearing vapor phase give rise to M- and W-type tetrad effects in the fluid and vapor phases, respectively (Monecke et al., 2011; Tang and Zhang, 2015). The fluid phase interacts with the early crystallized minerals, which induces similar tetrad effects in the latter as those of the former. This mechanism is denied by the M-type tetrad effect in the zircon PAs from Zones III and V (Fig. 4b–c). In addition, the common absence of a negative Ce anomaly in the zircon MAs from Zones II, III and V indicates that the metamict zircons are less altered by the late fluid phase.

(4) Immiscibility between silicate melt and hydrosaline melt/fluid before the formation of pegmatite-forming melt. This mechanism proposes that the hydrosaline brine characterized by the W-type tetrad effect separates from the parental granitic melt, which induces the M-type tetrad effect in the residual melt and its

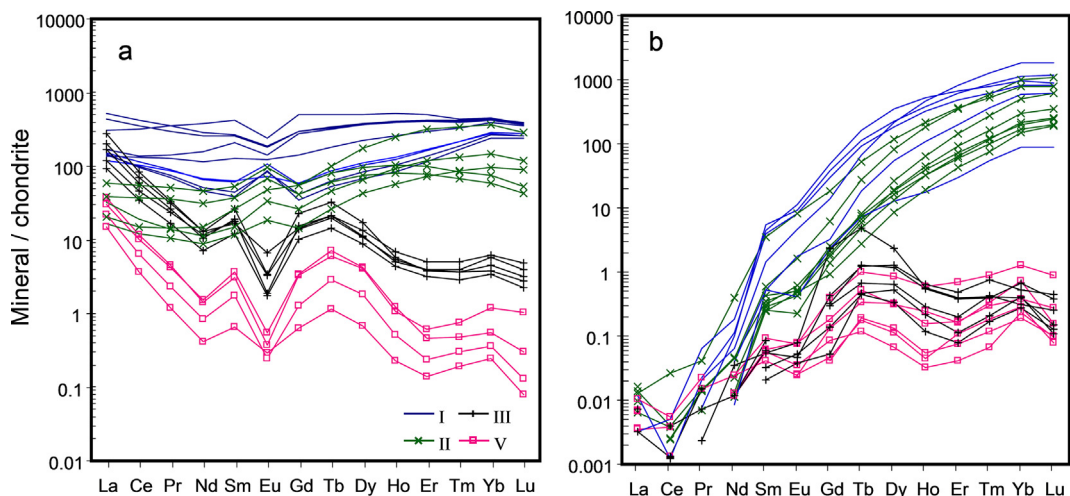


Fig. 6. Chondrite-normalized REE patterns of apatite (a) and spessartite (b) from Zones I, II, III and V of the Kelumute No. 112 pegmatite.

fractionated production, i.e., pegmatite-forming melt (Liu and Zhang, 2005; Cao et al., 2013). This mechanism is excluded by the general absence of lanthanide tetrads in zircons, spessartite and apatite from Zone II. It is also difficult to interpret the varying tetrad effects and Y/Ho ratios in zircons from Zone II to Zones III, V and VI.

- (5) Immiscibility between fluoride and silicate melts during the melt fractionation process (Veksler et al., 2005; Badanina et al., 2006; Peretyazhko and Savina, 2010). This mechanism suggests that the formation of fluoride melt and its preferential incorporation of REEs, especially Nd, Gd, Ho, Er and Lu, give rise to the W-type tetrad effect and subchondritic Y/Ho ratios in fluoride melt and the M-type tetrad effect and suprachondritic Y/Ho ratios in conjugated silicate melt (Veksler et al., 2005). We consider this mechanism more suitable for the fractionation of REEs in zircons from the No. 112 pegmatite based on the following evidence.

First, the immiscibility between fluoride and silicate melts has been observed both in experiments (Veksler et al., 2005, 2012; Dolejš and Baker, 2007a; Alferyeva et al., 2011) and in natural samples (Badanina et al., 2006; Peretyazhko and Savina, 2010; Vasyukova et al., 2014). Experiments on liquid immiscibility have demonstrated that REEs preferentially partition in fluoride melts rather than silicate melts (Veksler et al., 2005, 2012), and La, Nd, Gd, Ho and Lu show larger partitioning coefficients than their neighboring elements in fluoride melts, which induces the depletion and fractionation of REEs in silicate melts (Veksler et al., 2005). Immiscible fluoride melts, including Ca-F, Mg-F and Al-F fluorides, have all been proven to induce the M-type tetrad effect and depletion of REEs in conjugated silicate melts (Veksler et al., 2005; Peretyazhko and Savina, 2010), indicating the formation of fluoride melts is significant to generating the lanthanide tetrad effect. In the No. 112 pegmatite, a certain amount of fluorine is presented by the general occurrence of fluorapatite and fluoro-muscovite and the local occurrence of topaz and cryolite (Table 1). Although the required F abundance for immiscibility between fluoride and silicate melts is high to 4–5 wt% (Dolejš and Baker, 2007a,b), a high abundance of Li can serve to reduce the required F concentration (Veksler et al., 2005, 2012; Vasyukova et al., 2014). In addition, the constitutional zone refining process in pegmatite-forming melt is helpful for the concentration of incompatible elements and flux components in the local boundary layer melt (London, 2008), which facilitates the enrichment of F and the occurrence of liquid immiscibility. We suggest that the immiscibility between fluoride and silicate melts in the No. 112 pegmatite-forming melt was almost simultaneous with the crystallization of Zone III. This suggestion is consistent with the significant REE variations, including the increasing M-type tetrad effect and Y/Ho ratios (Fig. 5a) and decreasing REE contents in zircons (Fig. 5b) from Zone III, which is characterized by highly concentrated Li (spodumene) and F (topaz and cryolite) (Table 1).

Second, REEs-rich fluoride melts are commonly presented as inclusions and found at the microscopic scale (Veksler et al., 2005; Peretyazhko and Savina, 2010; Vasyukova et al., 2014) because of their relatively small quantity, high mobility, and chemically unstable nature (Veksler et al., 2005). In the No. 112 pegmatite, plenty of melt-fluid inclusions hosted by spodumene are observed in Zone III. They commonly consist of a silicate phase (spodumene and quartz), a fluid phase (liquid H₂O + CO₂ vapor) and an F-REE-rich phase (cryolite, monazite and/or xenotime) (Fig. 7a–c; Fig. 8). As we know, the LCT pegmatite affiliates with peraluminous melt and is commonly characterized by enrichments of Li, Ta, Cs, B, P and F, and depletions of Mg, Ca, Fe and REEs (Černý and Ercit, 2005; Černý et al., 2012); it is therefore difficult for REEs to reach their saturation abundance in most situations. These inclusions are suggested to be captured from the boundary layer melt by host minerals during the crystallization process (London, 2014), which indicates that the REEs and F are concentrated in the boundary layer melt. In addition, although the crystallization of REE-rich

minerals may induce the significant decrease in the REEs in zircons from Zones III and V, this process cannot give rise to the lanthanide tetrad effect and Y-Ho fractionation mentioned above. A positive correlation between the M-type tetrad effect and Y/Ho ratio is widely observed in granite and pegmatite (Irber, 1999; Liu and Zhang, 2005; Fig. 5a, this work), and a negative correlation between the REE content and Y/Ho ratio is also observed in this work (Fig. 5b). The mechanism must be responsible for not only increasing the lanthanide tetrad effect and Y-Ho ratios but also decreasing the REE content in zircons from Zones III and V. Therefore, only the immiscible REE-rich fluoride melt can be expected to induce the REE changes in Zone II to Zones III and V. We consider that the cryolite, monazite and xenotime minerals found in the inclusions represent the depolymerized products of REE-rich fluoride melts, and those inclusions may indicate the immiscibility of triple phases, i.e., a silicate melt, a fluoride melt and aqueous fluid. With experiments and natural samples, Veksler et al. (2002, 2004) documented the coexistence of three immiscible phases, including an aluminosilicate melt, a hydrosaline melt and an aqueous fluid, in a synthetic pegmatite. By inclusion studies, Thomas and co-workers proved the occurrence of three immiscible phases, i.e., a peraluminous and less water-rich melt, a conjugate water-rich peralkaline melt and a coexisting fluid phase, in pegmatite-forming melts (Thoams et al., 2006, 2011; Thomas and Davidson, 2008, 2012).

Comparatively, the zircons from Zone VI that formed at the hydrothermal stage have a similar lanthanide tetrad effect and Y/Ho ratio and a higher REE abundance relative to the zircons from Zones III and V that formed at the magmatic-hydrothermal stage (Fig. 5). This indicates that the fluid phase from which the zircons crystallized is rich in REEs. We suggest that the increase in REEs in zircons from Zone VI can be attributed to the formation of REECl²⁺ species in the Cl⁻-rich fluid exsolved from the No. 112 pegmatite-forming melt. As proved by previous experiments, REEs can bind with chlorine ions to form stable chloride species in brine (Luo and Byrne, 2001, 2007; Migdisov et al., 2009; Migdisov and Williams-Jones, 2008, 2014), and LREECl²⁺ species are more stable than HREECl²⁺ species under the same P-T conditions (Migdisov and Williams-Jones, 2008, 2009). Studies on REE ore deposits worldwide have demonstrated that REEs can be transported by the formation of REE-chloride species in saline fluid with moderate salinity and temperature conditions. Deposits such as the Bayan Obo ore deposits have been suggested to form under temperatures of 300–400 °C from brines containing 7–10 wt% NaCl eq. (Smith et al., 2000). The suggested ore-forming conditions for the Gallinas Mountains ore deposit are similar, with temperatures of 300–400 °C and 12–18 wt % NaCl eq. (Williams-Jones et al., 2000). In the magmatic-hydrothermal transition stage of the No. 112 pegmatite, the exsolved fluid was identified as an H₂O-NaCl-CO₂ phase based on fluid inclusions hosted by spodumene and quartz. The fluid phase is characterized by 18.1–12.9 wt% NaCl eq. at temperatures of 450–300 °C (Wu et al., 1994; Lv, 2013). Therefore, a certain amount of REEs, especially LREEs, may have been transported as REE-chloride species by the exsolution fluid due to the higher stability of the LREECl²⁺ species relative to the HREECl²⁺ species. It is consistent with the significant enrichment of LREEs in zircon MAs from Zone VI due to late alteration by the LREE-rich fluid phase (Fig. 4d).

From the above, the REE fractionation process in the No. 112 pegmatite-forming melt can be drawn as following. In the magmatic-hydrothermal transition stage, the incompatible REEs and fluxes of Li, F, P, Cl and H₂O are concentrated by the fractional crystallization of anhydrous minerals, such as alkaline feldspar and quartz. The continuous concentrations of these components induce immiscibility among a silicate melt, a fluoride melt and an aqueous fluid. The selective incorporation of REEs with fluorine ions generates the W-type tetrad effect and subchondritic Y/Ho ratios in the fluoride melt, which gives rise to the complementary M-type tetrad effect and suprachondritic Y/Ho ratios in the coexisting silicate melt and aqueous fluid. In addition, the preferential incorporation of REEs with fluorine and chlorine ions in the

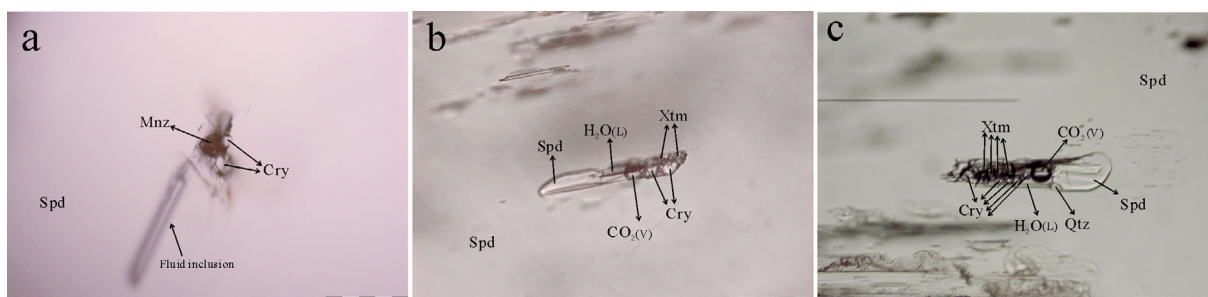


Fig. 7. Mineral and melt-fluid inclusions hosted by spodumene from the quartz-albite-spodumene zone (III) of Kelumute No.112 pegmatite. Coexisting of monazite, cryolite and fluid inclusion in spodumene (a); Melt-fluid inclusion composed of spodumene, quartz, H₂O liquid, CO₂ vapor, xenotime and cryolite (b and c). Abbreviation: Spd-spodumene, Qtz-quartz, Mnz-monazite, Cry-cryolite, Xtm-xenotime. V-vapor, L-liquid. Scale bars correspond to 100 μm .

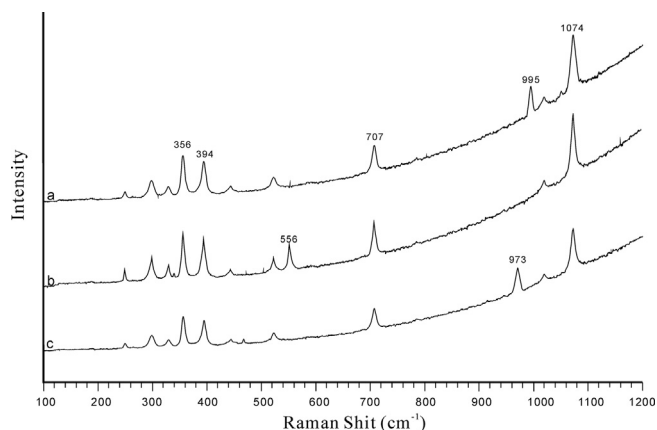


Fig. 8. Raman spectra of daughter minerals in inclusions hosted by spodumene from Zone III of the Kelumute No. 112 pegmatite. Spodumene is identified by Raman shift at 356 cm^{-1} , 394 cm^{-1} , 707 cm^{-1} and 1074 cm^{-1} . xenotime, cryolite and Monazite are identified by typical Raman shifts at (a) 995 cm^{-1} , (b) 556 cm^{-1} and (c) 973 cm^{-1} , respectively.

fluoride melt and exsolved fluid, respectively, result in the evident depletion of REEs in the silicate melt and zircons from Zones III and V.

5.3. Negative Ce anomaly in zircon

Until now, only one case of a terrestrial zircon with a negative Ce anomaly has been reported. However, the negative Ce anomaly in zircons from the Manaslu granite, Tibet, has been attributed to analytical errors (Barbey et al., 1995). Therefore, this work is the first identification of a negative Ce anomaly in terrestrial zircon. We propose three possible mechanisms responsible for the negative Ce anomaly in the zircons from Zone V, which formed at the late hydrothermal stage.

(1) Fractional crystallization of Ce-rich minerals prior to or during zircon saturation.

Ce-rich minerals, such as fluorocerite-(Ce), bastnaesite-(Ce), and monazite, can significantly deplete Ce from the bulk melt/fluid prior to or during zircon crystallization. However, these Ce-rich minerals are basically absent in the No. 112 pegmatite (Table 1). Although trace amounts of monazite and xenotime have been observed in inclusions from Zones III and V, the zircons from Zones III and V commonly have no negative anomaly. In addition, the experiments proved that the zircons from the three melts, which are saturated in LREE-bearing phases, show no clear differences between the calculated Ce anomalies and the positive Ce anomalies in the zircons from melts unsaturated in LREE-bearing phases, indicating the fractional crystallization of Ce-bearing minerals prior to or during zircon crystallization cannot induce the depletion of Ce relative to the neighboring La and Pr in zircon

(Burnham and Berry, 2012; Trail et al., 2012).

(2) Low oxygen fugacity (f_{O_2}) under reducing conditions.

Experiments and natural samples demonstrated that the magnitude of Ce anomalies in zircon is controlled by the abundance of Ce⁴⁺ in the melt/fluid and is related to the Ce⁴⁺ / Ce³⁺ ratio, which is a function of oxygen fugacity (Fujimaki, 1986; Ayers and Zhang, 2005; Hoskin and Schaltegger, 2003; Hoskin, 2005; Pettke et al., 2005; Burnham and Berry, 2012; Trail et al., 2012). In reducing conditions without the occurrence of Ce⁴⁺, zircons should have no evident Ce anomaly due to the consistency of the Ce³⁺ with the neighboring La³⁺ and Pr³⁺. For example, the zircons from the mesosiderite of Vaca Muerta 2 and from lunar rocks show no anomaly and a slightly negative Ce anomaly, respectively (Ireland and Wlotzka, 1992; Snyder et al., 1993). Experiments have demonstrated that the partitioning of REEs between zircons and fluids cannot induce a negative Ce anomaly (Fujimaki, 1986; Ayers and Zhang, 2005), and the Ce anomaly in zircons changes from a positive anomaly to no anomaly when the f_{O_2} of fluid phases decreases to near zero (Ayers and Zhang, 2005). Together, this evidence indicates that the extremely low f_{O_2} of the melts/fluids from which the zircon crystallized did not give rise to the evident negative Ce anomaly in the zircon.

(3) Preferential incorporation/adsorption of Ce in/by the Fe-Mn oxyhydroxides prior to or during the crystallization of zircon.

In nature, negative Ce anomalies are widely observed in fluid phases, such as in sea water, river water and mine drainage. The negative Ce anomalies in sea and river waters are attributed to the precipitation of CeO₂ due to the oxidation of Ce³⁺ to Ce⁴⁺ or the adsorption of Ce by Fe-Mn oxyhydroxides (Goldstein and Jacobsen, 1988; Elderfield et al., 1990). Negative Ce anomalies in volcano-hydrothermal fluids are attributed to the enhanced removal of Ce relative to La and Pr from the fluid by co-precipitation and/or adsorption onto the surface of authigenic Fe-Al oxyhydroxides (Inguaggiato et al., 2015). Experiments suggest that the preferential incorporation of Ce in Fe oxyhydroxides in an acidic fluid (pH \approx 4) can induce a negative Ce anomaly in the fluid (Bau, 1999). Similarly, experiments on the partitioning of REEs between Fe-Mn oxyhydroxide precipitates and NaCl solutions demonstrate that Ce has a higher partition coefficient than the neighboring elements La and Pr, which gives rise to significant positive Ce anomalies in Fe-Mn oxyhydroxides (Kawabe et al., 1999).

In the No. 112 pegmatite, a few Fe-Mn oxyhydroxides are observed (Table 1). They have been suggested to be the alteration products of Fe-Mn-bearing minerals by the exsolved fluid or precipitates from the exsolved fluid (Zou et al., 1981). According to the weight percentages of NaCl and CO₂ and the capture temperatures and pressures of the fluid inclusions obtained by previous works (Wu et al., 1994; Lv, 2013), the pH of exsolved fluid calculated by the calculation formula (Liu, 2011)

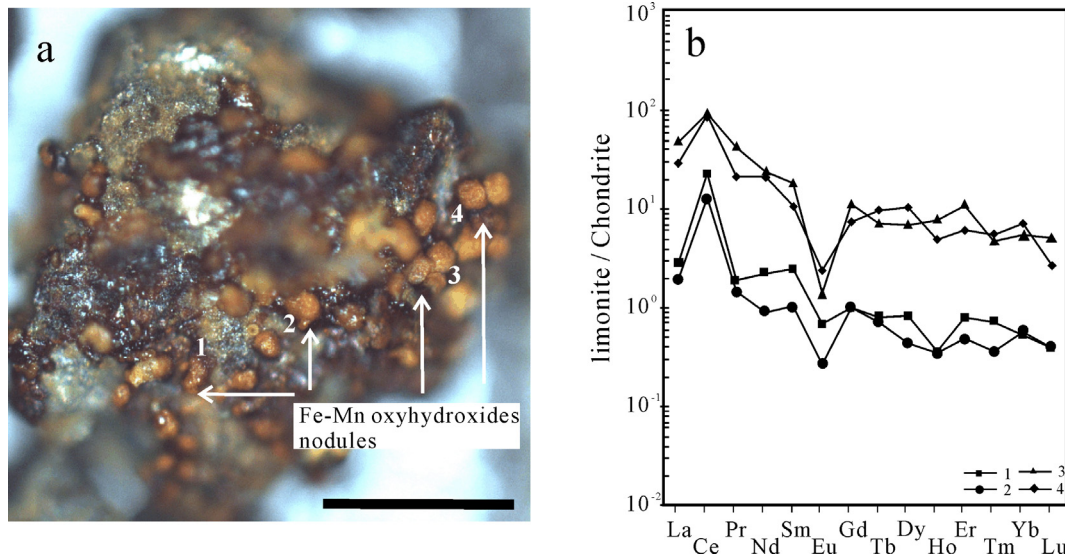


Fig. 9. Morphology (a) and chondrite-normalized REE patterns (b) of Fe-Mn oxyhydroxides nodules from Zone VI of Kelumute No.112 pegmatite. Limonite nodules show LREE-rich and significant Ce positive anomaly in their REE patterns. Scale bars correspond to 200 μm.

falls in the range of 3.8–4.6. Therefore, a fluid alteration process during the late hydrothermal stage could give rise to the generation of these secondary Fe-Mn-bearing minerals. In Zone VI, the Fe-Mn oxyhydroxides are observed in miarolitic cavities hosted by quartz. Their nodule shapes (Fig. 9a) indicate they precipitated from a hydrothermal fluid. The compositions of the Fe-Mn oxyhydroxides obtained from the in situ analysis by LA-ICPMS are characterized by a high FeO_T (78.24–96.01 wt%), varying MnO_T (1.62–16.79 wt%), low MgO, Al₂O₃ and SiO₂, and trace amount of REEs (15–130 ppm) (Table 4). In the REE patterns, an evident positive Ce anomaly and a lanthanide tetrad effect are observed (Fig. 9b). Therefore, it is reasonable to deduce that the negative Ce anomalies in the zircon PAs from Zone VI were induced by the preferential incorporation and/or adsorption of Ce in/by the Fe-Mn oxyhydroxides. In addition, the enhanced negative Ce anomalies in the zircon MAs are attributed to the alteration of primary zircons by Ce-depleted fluid during the late hydrothermal stage.

Although Fe-Mn oxyhydroxides are also observed in Zones II, III and V, the negative Ce anomaly is basically absent in the zircons from these zones. The zircon MAs from Zones II and III have weakened Ce anomalies (avg. of 1.53 and 1.25, respectively) compared to the PAs (avg. 2.01 and 1.50, respectively), indicating they may have been altered by fluid during the late hydrothermal stage. In Zone II, the negative Ce anomaly is only observed in a few of the zircon MAs (such as spots 8 and 16 from Zone II, Table 3), which indicates that only the intense alteration of the highly metamict area of zircon can change a Ce anomaly from positive to negative. The zircon PAs from these zones commonly have a positive Ce anomaly due to their (1) crystallization prior to the generation of Fe-Mn oxyhydroxides and (2) stable structure, which resists fluid alteration during the late hydrothermal stage. Fe-Mn oxyhydroxides are prevalent in nature, but they are mostly formed by supergene weathering under low temperatures (< 100 °C). In addition, Zr has a very low abundance in natural aqueous fluids, and the saturation of zircon is far prior to the formation of Fe-Mn oxyhydroxides in igneous rocks. All these may be the reasons why negative Ce anomalies are rarely observed in zircon. We declare that the mechanism for negative Ce anomalies in terrestrial zircon that was proposed in this work is just one possibility, because the phenomenon has not yet been proved and studied. Thus, this phenomenon must be studied in the future.

6. Conclusions

Based on the REE study of the three types of zircons from four mineral texture zones of the Kelumute No. 112 pegmatite, the following conclusions can be drawn:

- (1) REEs are significantly fractionated from the magmatic stage to hydrothermal stage of the No. 112 pegmatite-forming melt. The significant M-type tetrad effect and suprachondritic Y/Ho ratios in the zircons from Zones III, V and VI were induced by the selective incorporation of REEs in the immiscible fluoride melt;
- (2) The REE differentiation indicates that liquid immiscibility among a silicate melt, a fluoride melt and an aqueous fluid occurred during the magmatic-hydrothermal transition stage;
- (3) A negative Ce anomaly was identified for the first time in the terrestrial zircon from Zone VI of the No. 112 pegmatite and was attributed to the preferential incorporation and/or adsorption of Ce in/by the Fe-Mn oxyhydroxides prior to or during the crystallization of zircon in the hydrothermal stage.

Acknowledgments

We thank Profs Xiaoming Liu and Honglin Yuan from and Drs. Tao Han and Zhi-Hui Dai from IGCAS for their assistance with the LA-ICPMS analyses. Editor-in-chief Mei-Fu Zhou, Editor Ke-Da Cai, Miss Diane Chung and two anonymous reviewers are appreciated for their positive attitudes at work and constructive comments to help us improve the manuscript. This project was supported by the (Grant No. and 41372104) and funds from the Science and Technology Agency of Guizhou province, China (Grant No.).

References

- Alferyeva, Y.O., Gramenitskii, E.N., Shchekina, T.I., 2011. Experimental study of phase relations in a lithium-bearing fluorine-rich haplogranite and nepheline syenite system. *Geochem. Int.* 49, 676–690.
- Anckiewicz, R., Oberli, F., Burg, J.P., Villa, I.M., Gunther, D., Meier, M., 2001. Timing of normal faulting along the Indus Suture in Pakistan Himalaya and a case of major 231Pa/235U initial disequilibrium in zircon. *Earth Planet. Sci. Lett.* 191, 101–114.
- Ayers, J.C., Zhang, L., 2005. Zircon/fluid trace element partitioning. Abstract for Fall 2005.
- Badanina, E.V., Trumbull, R.B., Dulski, P., Wiedenbeck, M., Veksler, I.V., Syritso, F., 2006. The behavior of rare-earth and lithophile trace elements in rare-metal granites: a study of fluorite, melt inclusions and host rocks from the Khangilay complex, Transbaikalia, Russia. *Can. Mineral.* 44, 667–692.

- Bakker, R.J., Elburg, M.A., 2006. A magmatic-hydrothermal transition in Arkaroola (northern Flinders Ranges, South Australia): from diopside-titanite pegmatites to hematite-quartz growth. *Contrib. Mineral. Petrol.* 152, 541–569.
- Barbey, P., Allé, P., Brouand, M., Albarède, F., 1995. Rare-earth patterns in zircons from the Manaslu granite and Tibetan Slab migmatites (Himalaya): insights in the origin and evolution of a crustally-derived granite magma. *Chem. Geol.* 125, 1–17.
- Bau, M., 1996. Controls on the fractionation of isoivalent trace elements in magmatic and aqueous systems: evidence from Y/Ho, Zr/Hf, and lanthanide tetrad effect. *Contrib. Mineral. Petrol.* 123, 323–333.
- Bau, M., 1999. Scavenging of dissolved yttrium and rare earths by precipitating iron oxyhydroxide: experimental evidence for Ce oxidation, Y-Ho fractionation, and lanthanide tetrad effect. *Geochim. Cosmochim. Acta* 63, 67–77.
- Bau, M., Dulski, P., 1995. Comparative study of yttrium and rare-earth element behaviours in fluorine-rich hydrothermal fluids. *Contrib. Mineral. Petrol.* 119, 213–223.
- Black, L.P., Kamo, S.L., Allen, C.M., Davis, D.W., Aleinikoff, J.N., Valley, J.W., Mundil, R., Campbell, I.H., Korsch, R.J., Williams, I.S., Foudoulis, C., 2004. Improved $^{206}\text{Pb}/^{238}\text{U}$ microprobe geochronology by the monitoring of a trace-element-related matrix effect; SHRIMP, IDTIMS, ELA-ICP-MS and oxygen isotope documentation for a series of zircon standards. *Chem. Geol.* 205, 115–140.
- Burnham, A.D., Berry, A.J., 2012. An experimental study of trace element partitioning between zircon and melt as a function of oxygen fugacity. *Geochim. Cosmochim. Acta* 95, 196–212.
- Cao, M.J., Zhou, Q.F., Qin, K.Z., Tang, D.M., Evans, N.J., 2013. The tetrad effect and geochemistry of apatite from the Altay Koktokay No. 3 pegmatite, Xinjiang, China: implications for pegmatite petrogenesis. *Mineral. Petrol.* 107, 985–1005.
- Cherniak, D.J., Hanchar, J.M., Watson, E.B., 1997. Rare-earth diffusion in zircon. *Chem. Geol.* 134, 289–301.
- Černý, P., Eric, T.S., 2005. The classification of granitic pegmatites revisited. *Can. Mineral.* 43, 2005–2026.
- Černý, P., London, D., Novák, M., 2012. Granitic pegmatites as reflections of their sources. *Elements* 8, 289–294.
- Černý, P., Meintzer, R.E., Anderson, A.J., 1985. Extreme fractionation in rare-element granitic pegmatites; selected examples of data and mechanisms. *Can. Mineral.* 23, 381–421.
- Corfu, F., Hanchar, J.M., Hoskin, P.W., Kinny, P., 2003. Atlas of zircon textures. *Rev. Mineral. Geochem.* 53, 469–500.
- Dolejš, D., Baker, D.R., 2007a. Liquidus equilibria in the system $\text{K}_2\text{O-Na}_2\text{O-Al}_2\text{O}_3\text{-SiO}_2\text{-F}_2\text{O}_1\text{-H}_2\text{O}$ to 100 MPa: I. Silicate-fluoride liquid immiscibility in anhydrous systems. *J. Petrol.* 48, 785–806.
- Dolejš, D., Baker, D.R., 2007b. Liquidus equilibria in the system $\text{K}_2\text{O-Na}_2\text{O-Al}_2\text{O}_3\text{-SiO}_2\text{-F}_2\text{O}_1\text{-H}_2\text{O}$ to 100 MPa: II. Differentiation paths of fluorosilicic magmas in hydrous systems. *J. Petrol.* 48, 807–828.
- Dolejš, D., Štemprok, M., 2001. Magmatic and hydrothermal evolution of Li-F granites: Cinovec and Krásno intrusions, Krušné hory batholith, Czech Republic. *Bull. Geosci.* 76, 77–99.
- Duc-Tin, Q., Keppler, H., 2015. Monazite and xenotime solubility in granitic melts and the origin of the lanthanide tetrad effect. *Contrib. Mineral. Petrol.* 169, 1–26.
- Elderfield, H., Upstill-Goddard, R., Sholkovitz, E.R., 1990. The rare earth elements in rivers, estuaries, and coastal seas and their significance to the composition of ocean waters. *Geochim. Cosmochim. Acta* 54, 971–991.
- Fujimaki, H., 1986. Partition coefficients of Hf, Zr, and REE between zircon, apatite, and liquid. *Contrib. Mineral. Petrol.* 94, 42–45.
- Geisler, T., Rashwan, A.A., Rahn, M.K.W., Poller, U., Zwingmann, H., Pidgeon, R.T., Schleicher, H., Tomaschek, F., 2003. Low-temperature hydrothermal alteration of natural metamict zircons from the Eastern Desert, Egypt. *Mineral. Mag.* 67, 485–508.
- Goldstein, S.J., Jacobsen, S.B., 1988. Rare earth elements in river waters. *Earth Planet. Sci. Lett.* 89, 35–47.
- Hoskin, P.W.O., 2005. Trace element composition of hydrothermal zircon and the alteration of Hadean zircon from the Jack Hills, Australia. *Geochim. Cosmochim. Acta* 69, 637–648.
- Hoskin, P.W.O., Ireland, T.R., 2000. Rare earth element chemistry of zircon and its use as a provenance indicator. *Geology* 28, 627–630.
- Hoskin, P.W.O., Schaltegger, U., 2003. The composition of zircon and igneous and metamorphic petrogenesis. In: Hanchar, J.M., Hoskin, P.W.O., (Eds.), *Zircon Reviews in Mineralogy and Geochemistry*, Mineral. Soc. Am., Washington, vol. 53, pp. 27–62.
- Inguaggiato, C., Censi, P., Zuddas, P., Londoño, J.M., Chacón, Z., Alzate, D., Brusca, L., D'Alessandro, W., 2015. Geochemistry of REE, Zr and Hf in a wide range of pH and water composition: the Nevado del Ruiz volcano-hydrothermal system (Colombia). *Chem. Geol.* 417, 125–133.
- Irber, W., 1999. The lanthanide tetrad effect and its correlation with K/Rb, Eu/Eu*, Sr/Eu, Y/Ho, and Zr/Hf of evolving peraluminous granite suites. *Geochim. Cosmochim. Acta* 63, 489–508.
- Ireland, T.R., Wlotzka, F., 1992. The oldest zircons in the solar system. *Earth Planet. Sci. Lett.* 109, 1–10.
- Jahns, R.H., Burnham, C.W., 1969. Experimental studies of pegmatite genesis I: a model for the derivation and crystallization of granitic pegmatites. *Econ. Geol.* 64, 843–864.
- Kawabe, I., Ohta, A., Ishii, S., Tokumura, M., Miyauchi, K., 1999. REE partitioning between Fe-Mn oxyhydroxide precipitates and weakly acid NaCl solutions: convex tetrad effect and fractionation of Y and Sc from heavy lanthanides. *Geochim. J.* 33, 167–179.
- Lee, J.K., Williams, I.S., Ellis, D.J., 1997. Pb, U and Th diffusion in natural zircon. *Nature* 390, 159.
- Liu, B., 2011. Calculation of pH and Eh for aqueous inclusions as simple system. *Acta Petrologica Sinica* 27, 1533–1542.
- Liu, C.Q., Zhang, H., 2005. The lanthanide tetrad effect in apatite from the Altay No. 3 pegmatite, Xinjiang, China: an intrinsic feature of the pegmatite magma. *Chem. Geol.* 214, 61–77.
- Liu, Y.S., Hu, Z.C., Gao, S., Gunter, D., Xu, J., Gao, C.G., Chen, H.H., 2008. In situ analysis of major and trace elements of anhydrous minerals by LA-ICP-MS without applying an internal standard. *Chem. Geol.* 257, 34–43.
- London, D., 1986. The magmatic-hydrothermal transition in the Tanco rare-metal pegmatite: evidence from fluid inclusions and phase equilibrium experiments. *Am. Mineral.* 71, 376–395.
- London, D., 1992. The application of experimental petrology to the genesis and crystallization of granitic pegmatites. *Can. Mineral.* 30, 499–540.
- London, D., 2005. Granitic pegmatites: an assessment of current concepts and directions for the future. *Lithos* 80, 281–303.
- London, D., 2008. Pegmatites. *Can. Mineral. Special Publication* 10, 1–347.
- London, D., 2014. A petrologic assessment of internal zonation in granitic pegmatites. *Lithos* 184–187, 74–104.
- Lu, H.Z., Wang, Z.G., Li, Y.S., 1996. Magma/fluid transition and genesis of pegmatite dike No. 3 at Altay, Xinjiang. *Acta Mineral. Sin.* 16, 1–7 (In Chinese with English abstract).
- Luo, Y.R., Byrne, R.H., 2001. Yttrium and rare earth element complexation by chloride ions at 25 °C. *J. Solut. Chem.* 30, 837–845.
- Luo, Y.R., Byrne, R.H., 2007. The influence of ionic strength on yttrium and rare earth element complexation by fluoride ions in NaClO₄, NaNO₃ and NaCl solutions at 25 °C. *J. Solut. Chem.* 36, 673–689.
- Lv, Z.H., 2013. Magmatic-hydrothermal evolution and implications for origin of Kelumute No. 112 pegmatite, Xinjiang. Ph. D. thesis, Institute of Geochemistry, the Chinese Academy of Sciences. (in Chinese with English abstract).
- Lv, Z.H., Zhang, H., Tang, Y., Guan, S.J., 2012. Petrogenesis and magmatic-hydrothermal evolution time limitation of Kelumute No. 112 pegmatite in Altay, Northwestern China: evidence from zircon U-Pb and Hf isotopes. *Lithos* 154, 374–391.
- Masuda, A., 1975. Abundances of monoisotopic REE, consistent with the Leedy chondrite values. *Geochim. J.* 9, 183–184.
- Masuda, A., Kawakami, O., Dohmoto, Y., Takenaka, T., 1987. Lanthanide tetrad effect observed in leucogranite from China. *Geochim. J.* 23, 245–253.
- McLennan, S.M., 1994. Rare earth element geochemistry and the “tetrad” effect. *Geochim. Cosmochim. Acta* 58, 2025–2033.
- Migdisov, A.A., Williams-Jones, A.E., 2008. Speciation of REE (III) in chloride-, fluoride-, and sulphate-bearing solutions: solubility and spectroscopic studies. *Geochim. Cosmochim. Acta Supplement* 72, 626.
- Migdisov, A.A., Williams-Jones, A.E., 2014. Hydrothermal transport and deposition of the rare earth elements by fluorine-bearing aqueous liquids. *Miner. Deposita* 49, 987–997.
- Migdisov, A.A., Williams-Jones, A.E., Wagner, T., 2009. An experimental study of the solubility and speciation of the Rare Earth Elements (III) in fluoride- and chloride-bearing aqueous solutions at temperatures up to 300 °C. *Geochim. Cosmochim. Acta* 73, 7087–7109.
- Monecke, T., Dulski, P., Kempe, U., 2007. Origin of convex tetrads in rare earth element patterns of hydrothermally altered siliceous igneous rocks from the Zinnwald Sn-W deposit, Germany. *Geochim. Cosmochim. Acta* 71, 335–353.
- Monecke, T., Kempe, U., Monecke, J., Sala, M., Wolf, D., 2002. Tetrad effect in rare earth element distribution patterns: a method of quantification with application to rock and mineral samples from granite-related rare metal deposits. *Geochim. Cosmochim. Acta* 66, 1185–1196.
- Monecke, T., Kempe, U., Trinkler, M., Thomas, R., Dulski, P., Wagner, T., 2011. Unusual rare earth element fractionation in a tin-bearing magmatic-hydrothermal system. *Geology* 39, 295–298.
- Nasdala, L., Lengauer, C.L., Hanchar, J.M., Kronz, A., Wirth, R., Blanc, P., Kennedy, A.K., Seydoux-Guillaume, A.M., 2002. Annealing radiation damage and the recovery of cathodoluminescence. *Chem. Geol.* 191, 121–140.
- Nasdala, L., Pidgeon, R.T., Wolf, D., Irmer, G., 1998. Metamictization and U-Pb isotopic discordance in single zircons: a combined Raman microprobe and SHRIMP ion probe study. *Mineral. Petrol.* 62, 1–27.
- Nasdala, L., Zhang, M., Kempe, U., Panczer, G., Gaft, M., Andrut, M., Plötze, M., 2003. Spectroscopic methods applied to zircon. *Rev. Mineral. Geochem.* 53, 427–467.
- Pan, Y.M., 1997. Controls on the fractionation of isoivalent trace elements in magmatic and aqueous systems: evidence from Y/Ho, Zr/Hf, and lanthanide tetrad effect – a discussion of the article by M. Bau (1996). *Contrib. Mineral. Petrol.* 128, 405–408.
- Pan, Y.M., Breaks, F.W., 1997. Rare-earth elements in fluorapatite, Separation Lake area, Ontario; evidence for S-type granite-rare-element pegmatite linkage. *Can. Mineral.* 35, 659–671.
- Pearce, N.J.G., Perkins, W.T., Westgate, J.A., Gorton, M.P., Jackson, S.E., Neal, C.R., Chenery, S.P., 1997. A compilation of new and published major and trace element data for NIST SRM 610 and NIST SRM 612 glass reference materials. *Geostandard Newsletter* 21, 115–144.
- Peretyazhko, I.S., Savina, E.A., 2010. Tetrad effects in the rare earth element patterns of granitoid rocks as an indicator of fluoride-silicate liquid immiscibility in magmatic systems. *Petrology* 18, 514–543.
- Petteke, T., Audétat, A., Schaltegger, U., Heinrich, C.A., 2005. Magmatic-to-hydrothermal crystallization in the W-Sn mineralized Mole Granite (NSW, Australia): Part II: Evolving zircon and thorite trace element chemistry. *Chem. Geol.* 220, 191–213.
- Pidgeon, R.T., 1992. Recrystallization of oscillatory-zoned zircon: some geochronological and petrological implications. *Contrib. Mineral. Petrol.* 110, 463–472.
- Schaltegger, U., Fanning, C.M., Günther, D., Maurin, J.C., Schulman, K., Gebauer, D., 1999. Growth, annealing and recrystallization of zircon and preservation of monazite in high-grade metamorphism: conventional and in-situ U-Pb isotope, cathodoluminescence and microchemical evidence. *Contrib. Mineral. Petrol.* 134, 186–201.
- Sha, L.K., Chappell, B.W., 1999. Apatite chemical composition, determined by electron microprobe and laser-ablation inductively coupled plasma mass spectrometry, as a

- probe into granite petrogenesis. *Geochim. Cosmochim. Acta* 63, 3861–3881.
- Shannon, R.T., 1976. Revised effective ionic radii and systematic studies of interatomic distances in halides and chalcogenides. *Acta Crystallogr. Section A: Cryst. Phys., Diffraction, Theoretical General Crystallogr.* 32, 751–767.
- Smith, M.P., Henderson, P., Campbell, L.S., 2000. Fractionation of the REE during hydrothermal processes: constraints from the Bayan Obo Fe-REE-Nb deposit, Inner Mongolia, China. *Geochim. Cosmochim. Acta* 64, 3141–3160.
- Snyder, G.A., Taylor, L.A., Crozaz, G., 1993. Rare earth element selenochemistry of immiscible liquids and zircon at Apollo 14: an ion probe study of evolved rocks on the Moon. *Geochim. Cosmochim. Acta* 57, 1143–1149.
- Speer, J.A., 1982. Zircon. *Rev. Mineral.* 5, 67–112.
- Tang, Y., Zhang, H., 2015. Lanthanide tetrads in normalized rare element patterns of zircon from the Koktokay No. 3 granitic pegmatite, Altai, NW China. *Am. Mineral.* 100, 2630–2636.
- Thomas, R., Davidson, P., 2008. Water and melt/melt immiscibility, the essential components in the formation of pegmatites: evidence from melt inclusions. *Z. Geol. Wiss.* 36, 347–364.
- Thomas, R., Davidson, P., 2012. Water in granite and pegmatite-forming melts. *Ore Geol. Rev.* 46, 32–46.
- Thomas, R., Davidson, P., Schmidt, C., 2011. Extreme alkali bicarbonate- and carbonate-rich fluid inclusions in granite pegmatite from the Precambrian Rønne granite, Bornholm Island, Denmark. *Contrib. Mineral. Petrol.* 161, 315–329.
- Thomas, R., Kamenetsky, V.S., Davidson, P., 2006. Laser Raman spectroscopic measurements of water in unexposed glass inclusions. *Am. Mineral.* 91, 467–470.
- Touret, J.L.R., Smirnov, S.Z., Peretyazhko, I.S., Zagorsky, V.Y., Thomas, V.G., 2007. Magmatic/hydrothermal transition in tourmaline-bearing miarolitic pegmatites: hydrosaline fluids or silica gels. In: *International Symposium. Granitic Pegmatite, The State of the Art*, Porto, Portugal, pp. 92–93.
- Trail, D., Watson, E.B., Tailby, N.D., 2012. Ce and Eu anomalies in zircon as proxies for the oxidation state of magmas. *Geochim. Cosmochim. Acta* 97, 70–87.
- Van Lichtervelde, M., Melcher, F., Wirth, R., 2009. Magmatic vs. hydrothermal origins for zircon associated with tantalum mineralization in the Tanco pegmatite, Manitoba, Canada. *Am. Mineral.* 94, 439–450.
- Vasyukova, O., Williams-Jones, A.E., 2014. Fluoride-silicate melt immiscibility and its role in REE ore formation: evidence from the Strange Lake rare metal deposit, Québec-Labrador, Canada. *Geochim. Cosmochim. Acta* 139, 110–130.
- Veksler, I.V., Thomas, R., Schmidt, C., 2002. Experimental evidence of three coexisting immiscible fluids in synthetic granitic pegmatite. *Am. Mineral.* 87, 775–779.
- Veksler, I.V., 2004. Liquid immiscibility and its role at the magmatic-hydrothermal transition: a summary of experimental studies. *Chem. Geol.* 210, 7–31.
- Veksler, I.V., Dorfman, A.M., Kamenetskaya, M., Dulski, P., Dingwell, D.B., 2005. Partitioning of lanthanides and Y between immiscible silicate and fluoride melts, fluorite and cryolite and the origin of the lanthanide tetrad effect in igneous rocks. *Geochim. Cosmochim. Acta* 69, 2847–2860.
- Veksler, I.V., Dorfman, A.M., Dulski, P., Kamenetsky, V.S., Danyushevsky, L.V., Jeffries, T., Dingwell, D.B., 2012. Partitioning of elements between silicate melt and immiscible fluoride, chloride, carbonate, phosphate and sulfate melts, with implications to the origin of natrocarbonatite. *Geochim. Cosmochim. Acta* 79, 20–40.
- Wang, T., Tong, Y., Jahn, B.M., Zou, T.R., Wang, Y.B., Hong, D.W., Han, B.F., 2007. SHRIMP U-Pb Zircon geochronology of the Altai No. 3 Pegmatite, NW China, and its implications for the origin and tectonic setting of the pegmatite. *Ore Geol. Rev.* 32, 325–336.
- Wang, X.J., Zou, T.R., Yu, X.Y., Qiu, Y.Z., 1981. The mineralogy study of pegmatite in the Chinese Altai. *Scientific Publishing House, Beijing*, pp. 1–78 (in Chinese).
- Webster, J.D., Thomas, R., Rhede, D., Förster, H.J., Seltmann, R., 1997. Melt inclusions in quartz from an evolved peraluminous pegmatite: geochemical evidence for strong tin enrichment in fluorine-rich and phosphorus-rich residual liquids. *Geochim. Cosmochim. Acta* 61, 2589–2604.
- Williams-Jones, A.E., Samson, I.M., Olivo, G.R., 2000. The genesis of hydrothermal fluorite-REE deposits in the Gallinas Mountains, New Mexico. *Econ. Geol.* 95, 327–341.
- Wu, B.Q., Zou, T.R., 1989. The genesis of granitic pegmatites in Xinjiang Altai. *Mineral Geol. Xinjiang* 1, 60–70 (in Chinese).
- Wu, C.N., Zhu, J.C., Liu, C.S., 1994. A study on the inclusions in spodumenes from Altai pegmatite, Xinjiang. *Geotectonica et Metallonemia* 18, 353–362 (in Chinese with English abstract).
- Wu, C.Z., Liu, S.H., Gu, L.X., Zhang, Z.Z., Lei, R.X., 2011. Formation mechanism of the lanthanide tetrad effect for a topaz- and amazonite-bearing leucogranite pluton in eastern Xinjiang, NW China Zircon/rock partition coefficients of REEs, Y, Th, U, Nb, and Ta in granitic rocks: uses for provenance and mineral exploration purposes. *J. Asian Earth Sci.* 42, 903–916.
- Wu, Y.B., Zheng, Y.F., 2004. Genesis of zircon and its constraints on interpretation of U-Pb age. *Chin. Sci. Bull.* 49, 1554–1569.
- Yuan, H.L., Gao, S., Liu, X.M., Li, H.M., Günther, D., Wu, F.Y., 2004. Accurate U-Pb age and trace element determinations of zircon by laser ablation-inductively coupled plasma mass spectrometry. *Geoanal. Geostandard Res.* 28, 353–370.
- Zeng, L.J., Niu, H.C., Bao, Z.W., Yang, W.B., 2017. Chemical lattice expansion of natural zircon during the magmatic-hydrothermal evolution of A-type granite. *Am. Mineral.* 102, 655–665.
- Zhang, A.C., Wang, R.C., Jiang, S.Y., Hu, H., Zhang, H., 2004. Chemical and textural features of tourmaline from the spodumene-subtype Koktokay No. 3 pegmatite, Altai, northwestern China: a record of magmatic to hydrothermal evolution. *Can. Mineral.* 46, 41–58.
- Zhang, A.C., Wang, R.C., Xie, L., Hu, H., 2003. Hafnian zircon from the Koktokay No. 3 granitic pegmatite vein, Altai, NW China. *Acta Mineral. Sin.* 23, 327–332.
- Zhang, H., 2001. The geochemical behaviors and mechanisms of incompatible trace elements in the magmatic-hydrothermal transition system: a case study of Altai No. 3 pegmatite, Xinjiang. Ph. D. thesis, Institute of Geochemistry, the Chinese Academy of Sciences. (in Chinese with English abstract).
- Zhao, J.X., Cooper, J.A., 1993. Fractionation of monazite in the development of V-shaped REE patterns in leucogranite systems: evidence from a muscovite leucogranite body in central Australia. *Lithos* 30, 23–32.
- Zhao, Z.H., Xiong, X.L., Han, X.D., Wang, Y.X., Wang, Q., Bao, Z.W., Jahn, B.M., 2002. Controls on the REE tetrad effect in granites: evidence from the Qianlishan and Baerzhe Granites, China. *Geochem. J.* 36, 527–543.
- Zou, T.R., Yang, Y.Q., Cao, H.Z., Yao, Y.T., 1981. Study of the composition, mineralization and genesis of the No. 112 pegmatite, Xinjiang. Report. Chinese Academy of Geological Sciences (in Chinese).